Journal of *Marine Science and Engineering*

MDPI

Article

Prediction of Scale Effects on Tidal Turbines with the Reynolds Scaling Method

Gyeongseo Min [1], Kangmin Kim [1], Haechan Yun [1], Younguk Do [1], Weichao Shi [2], Daejeong Kim [3,*] and Soonseok Song [1,*]

[1] Department of Naval Architecture & Ocean Engineering, Inha University, Incheon 22212, Republic of Korea; gyeongseo6691@naver.com (G.M.); km060503@naver.com (K.K.); haechan7108@naver.com (H.Y.); d0ook@inha.edu (Y.D.)
[2] School of Engineering, Newcastle University, Newcastle upon Tyne NE1 7RU, UK; weichao.shi@newcastle.ac.kr
[3] Division of Navigation Convergence Studies, Korea Maritime & Ocean University, Busan 49112, Republic of Korea
* Correspondence: kdj4907@kmou.ac.kr (D.K.); s.song@inha.ac.kr (S.S.)

Abstract

Accurate power estimation is fundamental to effective tidal turbine design. While turbines are typically designed for specific Tip Speed Ratio (TSR) ranges, the Reynolds number (*Re*) can vary significantly even at a constant TSR depending on flow velocity and turbine scale. Such variations in *Re* can fundamentally alter the flow characteristics around the blades, directly impacting performance. Conventionally, *Re*-dependent lift and drag coefficients are incorporated into Blade Element Momentum Theory (BEMT) to address these variations, often supplemented by hub and tip loss corrections. However, since BEMT relies on two-dimensional airfoil characteristics, it may not fully capture the complex three-dimensional viscous effects that occur during actual operation. Therefore, this study employs three-dimensional CFD simulations to quantitatively evaluate *Re* effects on turbine performance. By quantifying power generation deviations across a broad *Re* spectrum, the results show that discrepancies at identical TSRs range from 0.312% to 7.32%. Notably, these differences stabilise near 1% when *Re* exceeds 1.0×10^7. Furthermore, the underlying causes of these scale effects were identified by decomposing the torque into shear and pressure components. These quantified indicators provide a practical basis for incorporating Reynolds number effects into the turbine design process, thereby contributing to more accurate full-scale performance prediction.

Keywords: tidal turbine; blade element momentum theory; computational fluid dynamics (CFD); scale effects; Reynolds scaling method

Academic Editor: Fuping Gao

Received: 17 April 2026
Revised: 30 April 2026
Accepted: 6 May 2026
Published: 12 May 2026

1. Introduction

As climate change and the depletion of fossil fuels become more pressing issues, the need for alternative energy sources to replace fossil fuels has increased. Consequently, the importance of renewable energy sources, such as wind and tidal power, has risen in recent times. Tidal current turbines generate power by converting the kinetic energy of the current flow into electricity. Among these, tidal power is gaining attention as an environmentally friendly marine energy source that can generate electricity using the flow of ocean currents. Tidal turbines come in two types, horizontal and vertical axis. Horizontal and vertical axis turbines are classified based on whether they rotate parallel or perpendicular to the tidal

flow. Among them, horizontal axis tidal turbines (HATTs) are the more developed and can be utilised to obtain a large quantity of energy from marine currents [1]. They are widely used in various countries, including the United Kingdom (Seagen), Canada (Clean Current turbine), France (HydroHelix) and many others.

Recently, as tidal turbines have gained increasing attention, research has been conducted across various fields [2,3]. In the planning process for tidal turbines, critical factors such as depth and current speed need to be considered. Since tidal turbines are greatly influenced by their location, it is important to design tidal turbines that are suitable for the intended site and to predict their performance accurately. There are various methods available for designing tidal turbines and assessing their performance.

Firstly, the performance of tidal turbines can be predicted through experimental methods. There were various previous studies on tidal turbines conducted through experimental approaches [4,5]. For example, in a previous study [6], experiments were conducted to examine the wake characteristics and hydrodynamic performance of a horizontal axis tidal turbine model under yawed inflow conditions. This study found patterns in the wake behaviour, such as the dependence on the turbine yaw angle and the reduction in wake recovery with increased yaw. In another experimental study [7], it was revealed that surface waves did not affect the average loads and power output but caused severe periodical oscillations in experiments conducted in a towing tank. Besides, non-dimensional response amplitude operators (RAOs) of thrust and torque were proved to be sensitive to the submergence of the turbine.

Secondly, Blade Element Momentum Theory (BEMT) has been widely adopted as an efficient and reliable approach for tidal turbine design and performance assessment. The method offers efficient computational performance along with high accuracy, making it an effective approach for both design and performance prediction. In previous studies, BEMT was used to measure the efficiency of tidal turbines as well as various types of tidal turbines. In a previous study [8], existing expressions established through experiments and Computational Fluid Dynamics (CFD) for factors such as inlet efficiency, diffuser efficiency, and base pressure were adapted to be suitable for a bidirectional duct. These adapted expressions were then used to determine the axial induction factor. The ducted BEMT has shown significantly lower computational requirements with reliable results. In related research [9], BEMT results were used to identify the optimum blade design for use in the CFD model and for manufacturing in the workshop. The optimum chord length distribution and twist distribution were determined by comparing BEMT results.

However, there are some challenges to using BEMT. Airfoil evaluation is an essential process in BEMT analysis. The 2D model of the airfoil is commonly analysed using Xfoil, which is a practical resource for assessing airfoils with respect to lift coefficient (C_L), drag coefficient (C_D), and pressure coefficient (C_{Pmin}). It is important to note that the Reynolds number is typically considered only for 2D airfoils, which may not fully capture the complexities of 3D tidal turbine performance.

Many studies have been conducted to overcome the challenges in traditional BEMT methods. For instance, a study [10] suggested a BEMT performance model that is extended by Prandtl corrections for losses at the blade tip and hub. The Prandtl tip and hub loss corrections were found to improve accuracy when compared to a lifting line theory model. Moreover, these corrections require only a small computational cost. Similarly, another study [11] proposed 3D corrections to improve the accuracy of the Blade Element Momentum (BEM) results. Because BEM theory is two dimensional, it is difficult to account for three-dimensional effects. As a result, it shows significant discrepancies in flow quantities compared to measured turbine data, especially in areas with substantial variations in blade circulation. Furthermore, recent research [12] developed a BEMT model for high solidity

and highly loaded vertical axis tidal turbine rotors which traditional BEMT models are incapable of modelling. The double multiple stream-tube model employs a graphical approach for determination of axial induction factors rather than the iterative approach used in traditional BEMT models.

Finally, there is a method for evaluating turbine capability using CFD. Recently, analyses of tidal turbines using CFD have also been conducted in various fields. In one study [13], the impact of biofouling on power generation in tidal turbines was quantified. From another perspective, a computational study [14] presented a computational free surface flow framework that facilitates 3D, time-dependent simulations of HATTs. These free surface flow simulations were validated with experiments and showed good agreement with the experiment data. Beyond these, previous studies have also investigated tidal turbines in relation to sediment transport and free surface effects using CFD [15,16].

Regarding the differences between BEMT and CFD, CFD requires significantly more computational resources than BEMT. However, CFD offers the advantage of capturing effects related to Reynolds numbers. Despite numerous efforts to bridge the limitations of BEMT, challenges persist in accurately accounting for the influence of the Reynolds number in BEMT models.

There are previous studies regarding the effects of the Reynolds number on tidal turbines [17,18]. Specifically, it was demonstrated in a study [19], using CFD that the cross-flow tidal turbine at full scale achieves higher power coefficients than an equivalent lab scale model. Additionally, above a Reynolds number of approximately 350,000, the power coefficients across all operating conditions become proportional. In this study, the Reynolds number varied by adjusting the TSR, diameter, and flow velocity to obtain these results. Similarly, through experiments and CFD, a study [20] revealed that the performance characteristics of a HATT, such as power and thrust coefficients, remain unaffected by changes in Reynolds numbers greater than 5.0×10^5.

Since turbine output varies with the Reynolds number, the influence of the Reynolds number is a critical factor in accurately predicting the efficiency of tidal turbines. Based on these previous studies, the aim of this study is to quantitatively assess the effects of the Reynolds number on tidal turbine performance and to systematically evaluate the performance deviations resulting from Reynolds number variations. In this study, CFD using Reynolds-averaged Navier–Stokes (RANS) was developed to assess the effect of Reynolds number on HATT characteristics. Additionally, the BEM method was used for simulating horizontal axis turbines using Qblade (version 2.0.6.4). The software Qblade is mainly used in the design of wind turbine blades; however, it is a program that has been applied to tidal turbines by modifying fluid properties and other parameters [21]. In Qblade, lift and drag coefficients for each airfoil section are derived using the integrated Xfoil solver, which accounts for Reynolds number-dependent characteristics. By comparing BEMT and CFD, the present study aims to quantify the Reynolds number effects on tidal turbine performance.

This paper is organised as follows: The methodology of the numerical study is explained in Section 2, which covers mathematical formulation and simulation conditions. In Section 3, the verification and validation of numerical simulations are assessed. Accordingly, Reynolds number effects on various turbine sizes are evaluated using virtual fluid in Section 4. Moreover, the reasons for different turbine performance at different scales are revealed.

2. Methodology

2.1. Mathematical Formulation

The performance of a tidal turbine was evaluated using a CFD model. STAR-CCM+ (version 19.02.012) was used to implement the RANS-based CFD model for turbine performance evaluation. The following two equations represent the averaged continuity and momentum equations for incompressible flows in tensor notation and Cartesian coordinates [22].

$$\frac{\partial(\rho\overline{u}_i)}{\partial x_i} = 0 \tag{1}$$

$$\frac{\partial(\rho\overline{u}_i)}{\partial t} + \frac{\partial}{\partial x_j}\left(\rho\overline{u}_i\overline{u}_j + \rho\overline{u_i'u_j'}\right) = -\frac{\partial\overline{p}}{\partial x_i} + \frac{\partial\overline{\tau}_{ij}}{\partial x_j} \tag{2}$$

In these equations, ρ is density, $\overline{u}_i$ is averaged velocity, $\overline{u_i'u_j'}$ is the Reynolds stress, $\overline{p}$ is the averaged pressure, and $\overline{\tau}_{ij}$ represents the components of the mean viscous stress tensor. For a Newtonian fluid, this viscous stress can be derived as

$$\overline{\tau}_{ij} = \mu\left(\frac{\partial u_i}{\partial x_j} + \frac{\partial u_j}{\partial u_i}\right) \tag{3}$$

where μ denotes the dynamic viscosity.

In CFD solver (Star-ccm+ version 19.02.012), the finite volume method was used by discretising the computational domain. The momentum equations were solved by a second-order upwind convection scheme in the computational domain. Additionally, a predictor–corrector method was used to couple the continuity and momentum equations.

In these simulations, turbulence effects were predicted using the shear stress transport (SST) $k-\omega$ turbulence model. The SST $k-\omega$ turbulence model is an improved prediction model that combines the advantages of the $k-\omega$ and $k-\varepsilon$ turbulence models. This model increases the accuracy of near-wall treatment by using the $k-\omega$ formulation in the boundary layer and the $k-\varepsilon$ behaviour in the free stream [23].

2.2. Geometry and Simulation Conditions

In this research, a full-scale HATT geometry with a 20 m rotor diameter, as shown in Table 1, was used for simulations with various rotor sizes, and a 1:50 model-scale HATT was used for validation comparison with experimental data. The HATT model employed in this study was validated through experimental and model-scale CFD studies conducted in previous studies [24,25]. Accordingly, validation was performed at the model scale, followed by full-scale CFD simulations in this paper. The specifications of the full-scale HATT used in the simulations can be found in Table 1 and Figure 1. Additionally, the blade used in the BEMT simulation is the same as that used in the CFD simulation. Table 2 and Figure 2 present the main particulars of the blade and the airfoil used. The reason for using this specific airfoil and blade configuration is to enable the comparison and validation between existing experimental data and CFD results by employing the same turbine geometry that was used in previous studies.

Table 1. Main dimension of HATT.

Parameters	
Diameter	20 m
Number of blades	3
Immersion of shaft	20 m
Rotation rate (RPM)	12
Current speed	3.2 m/s

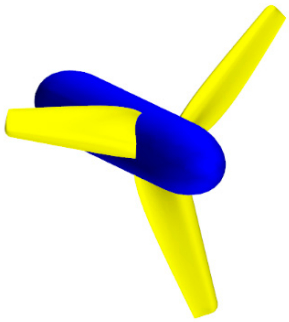

Figure 1. Geometry of the HATT.

Table 2. Main particulars of tidal turbine model.

r/R	0.2	0.3	0.4	0.5	0.6	0.7	0.8	0.9	1
Chord length (mm)	64.35	60.06	55.76	51.47	47.18	42.88	38.59	34.29	30
Pitch angle (deg.)	35.33	23.33	15.83	12.33	10.33	8.83	7.93	7.03	6.33

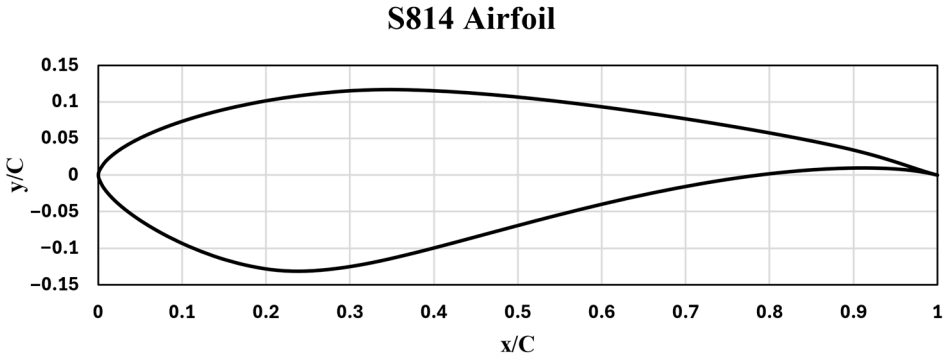

Figure 2. S814 section profile.

To estimate the scale effects on tidal turbines, simulations were conducted using turbines of various rotor diameters: 0.4 m, 4 m, 8 m, 12 m, 20 m, and 40 m. The reason for selecting these various turbine sizes was to cover a comprehensive range that encompasses both large- and small-scale turbines. Simulations for these different turbine sizes were performed only using a 20 m full-scale turbine geometry with a virtual fluid. To match the Reynolds number for different turbine sizes on the same scale of geometry, a virtual fluid with a constant inflow velocity (V_{in} = 3.2 m/s) was used, adjusting the dynamic viscosity according to the size of each turbine. The feasibility of using the virtual fluid was validated, as comparative results with a real fluid for propeller characteristics were all in good agreement at full-scale in a previous study [26]. The turbines were tested at TSRs ranging from 1 to 8, and during this process, the rotational speed (ω) was modified according to the changes in TSR. The tip speed ratio, TSR is represented as

$$TSR = \frac{\omega R}{V_{in}} \tag{4}$$

where ω is the rotational speed (rad/s), R is the blade radius of the turbine, and V_{in} is the incoming current velocity.

Through each simulation, the power coefficient and the thrust coefficient were measured, which are expressed as

$$C_p = \frac{P}{\frac{1}{2}\rho A_T V_{in}^3} \tag{5}$$

$$C_T = \frac{T}{\frac{1}{2}\rho A_T V_{in}^2} \tag{6}$$

where P is the power, T is the thrust, and A_T is the swept area of turbine.

2.3. Computational Domain and Boundary Conditions

In Figure 3, the computational domain and the boundary conditions used in the CFD simulation are shown. The domain was divided into two regions. The first is the rotating region, which represents the area where the turbine rotates and is coloured yellow in Figure 3. The second is the stationary region, located outside the rotating region. The stationary region replicates the cavitation tunnel experiment conducted by the previous study [24]. The boundary conditions applied in the simulations are as follows. At the inlet, a uniform velocity of 3.2 m/s was prescribed in the streamwise direction. At the outlet, a pressure outlet boundary condition with a constant static pressure was imposed. In the stationary region, a no-slip wall condition was applied, except at the inlets and outlets, where it was assumed that the boundary layer effects of the surrounding walls were negligible for predicting turbine behaviour. At the interface between the rotating and stationary regions, the MRF approach was applied to exchange flow variables between the two reference frames.

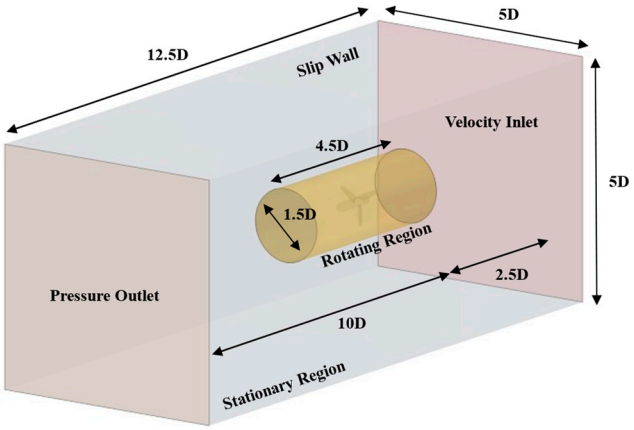

Figure 3. Domain and boundary conditions of the simulations.

The MRF (Multiple Reference Frame) approach provides a steady-state approximation by fixing the relative position between rotating and stationary region. At the interface between regions assigned stationary and rotating reference frames, local variable values are transformed from one reference frame to another on a cell-by-cell basis. Since no actual mesh motion is involved, the position of the moving object relative to the neighbouring region remains unchanged. In steady-state simulations, because there is no mesh motion caused by moving the blades, less computational power is required compared to unsteady motion (e.g., the Sliding Mesh), which reduces computation time. As demonstrated by other studies using the MRF approach [27,28], the authors do not expect this study to show significant difference compared to using the unsteady method.

2.4. Mesh Generation

Mesh generation was conducted using the built-in automated mesh tool provided by STAR-CCM+ with the trimmed cell meshes. As shown in Figure 4, local mesh refinement was applied to the area around the blade and the swept area to enhance the accuracy of the calculations by using finer meshes. Additionally, the base size of the mesh was set to diameter divided by 24, and in the swept area, one-fourth of the base was used.

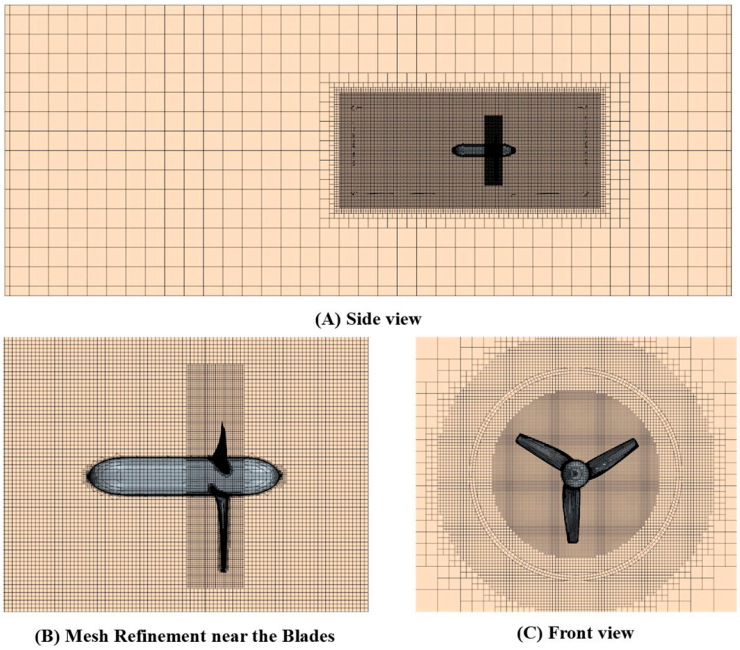

Figure 4. Grid system of simulations.

The prism layer meshes were employed for near-wall refinement. To ensure the accuracy of both the full-scale and model-scale simulations, the first layer thickness of the prism layer was adjusted so that the y+ values were above 30 in the full-scale simulations and below 1 in the model-scale simulations. Moreover, the total thickness of the prism layer and the size of the first cell were kept the same to maintain consistency across simulations using virtual fluid for turbines of different sizes. The number of prism layers was varied to achieve the same y+ value.

3. Verification and Validation Studies

3.1. Verification Study

A verification study was carried out to quantify the numerical uncertainty associated with the CFD simulations. The accuracy of these simulations was evaluated using the Grid Convergence Index (GCI), which was based on Richardson's extrapolation method [29]. According to the approach outlined by a previous study [30], the apparent order, denoted as p_a, is determined by

$$p_a = \frac{1}{\ln(r_{21})}\left|\ln\left|\frac{\varepsilon_{32}}{\varepsilon_{21}}\right| + q(p_a)\right| \tag{7}$$

$$q(p_a) = \ln\left(\frac{r_{21}^{p_a} - s}{r_{32}^{p_a} - s}\right) \tag{8}$$

$$s = sign\left(\frac{\varepsilon_{32}}{\varepsilon_{21}}\right) \tag{9}$$

In these equations, the terms r_{21} and r_{32} represent grid refinement factors, which are evaluated by the expression $r_{21} = \sqrt[3]{N_1/N_2}$ for a spatial convergence test of a 3D model. In this context, N denotes the cell number of the simulations. The differences ε_{32} and ε_{21} are defined as $\varepsilon_{32} = \phi_3 - \phi_2$ and $\varepsilon_{21} = \phi_2 - \phi_1$, where ϕ_k denotes the key variables. In this study, the key variables ϕ_k are the power coefficient (C_p) or the thrust coefficient (C_T).

The extrapolated value is calculated by

$$\phi_{ext}^{21} = \frac{r_{21}^{p}\phi_1 - \phi_2}{r_{21}^{p} - 1} \tag{10}$$

The approximate relative error, e_a^{21}, and extrapolated relative error, e_{ext}^{21}, are evaluated by

$$\phi_{ext}^{21} = \frac{r_{21}^p \phi_1 - \phi_2}{r_{21}^p - 1} \tag{11}$$

$$e_{ext}^{21} = \left| \frac{\phi_{ext}^{21} - \phi_1}{\phi_{ext}^{21}} \right| \tag{12}$$

Finally, the fine-grid convergence index is determined by

$$GCI_{fine}^{21} = \frac{1.25 e_a^{21}}{r_{21}^p - 1} \tag{13}$$

Three different grid simulations, referred to as fine, medium, and coarse meshes, were used to evaluate the numerical uncertainty. These meshes correspond to total cell numbers of N_1, N_2, and N_3, respectively. Table 3 shows the required variables for the spatial convergence test. The power coefficient, C_p, and thrust coefficient, C_T at TSR 4 were used as variables for uncertainty verification at the model scale (D = 0.4 m). The numerical uncertainties using the fine mesh are 0.37% and 0.27%. For predicting accurate turbine efficiency, the fine mesh was used in the simulations, which were conducted on full-scale simulations under virtual fluid conditions.

Table 3. Uncertainty estimation from spatial convergence studies.

	C_p	C_T
N_1	2,531,253	2,531,253
N_2	1,654,709	1,654,709
N_3	1,040,788	1,040,788
r_{21}	1.53	1.53
r_{32}	1.59	1.59
ϕ_1 (Fine)	4.6945×10^{-1}	8.3373×10^{-1}
ϕ_2 (Medium)	4.6741×10^{-1}	8.2918×10^{-1}
ϕ_3 (Course)	4.6162×10^{-1}	8.3060×10^{-1}
ε_{32}	-5.79×10^{-3}	1.421×10^{-3}
ε_{21}	-2.04×10^{-3}	-4.55×10^{-3}
s	1	-1
e_a^{21}	4.341×10^{-3}	5.463×10^{-3}
q	-1.3451×10^{-1}	-8.969×10^{-2}
p_a	2.1395	2.9511
ϕ_{ext}^{21}	4.708×10^{-1}	8.336×10^{-1}
e_{ext}^{21}	2.919×10^{-3}	2.175×10^{-3}
GCI_{fine}^{21}	0.37%	0.27%

3.2. Validation Study

Figures 5 and 6 show a comparison of the power coefficients and thrust coefficients between the CFD and experimental data [25]. As shown in the figures, the results between the CFD and EFD are in good agreement across the entire measured TSR range, with only slight differences. In the authors' opinion, considering the experimental errors and numerical errors, these differences are negligible. An important consideration is the Reynolds numbers for the experiment and simulation, based on chord length at 0.7 R and the relative velocity ($V_R = \sqrt{V_A^2 + (0.7\omega D)^2}$). These Reynolds numbers range from $1.3 - 8.5 \times 10^5$ as the TSR varies from 1 to 8. Although experimental uncertainties were not reported in the previous study, the numerical uncertainty of the present CFD simulations is confirmed to be less than 1%, as shown in Table 3.

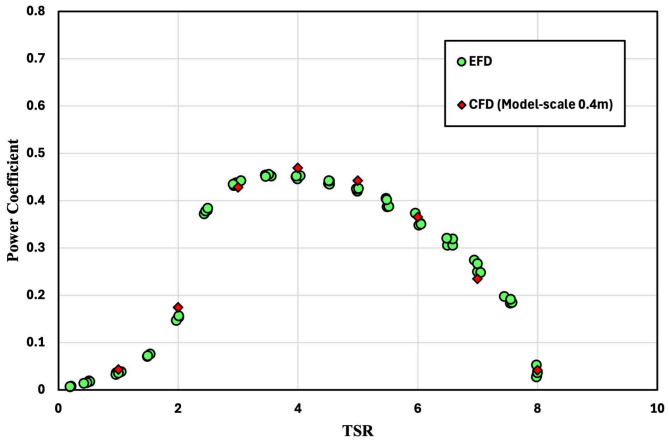

Figure 5. Comparison of the power coefficients between EFD and CFD.

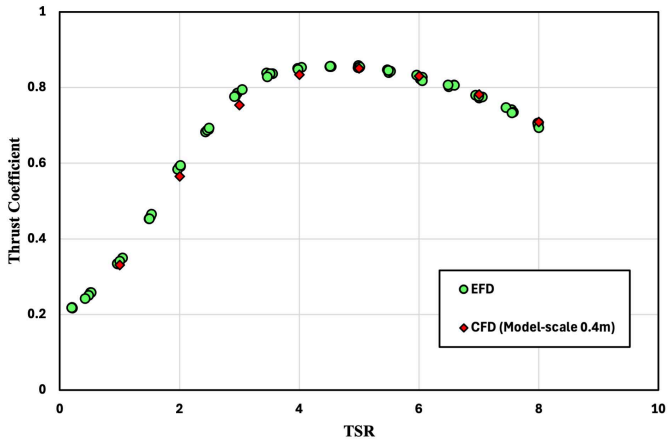

Figure 6. Comparison of the thrust coefficients between EFD and CFD.

4. Result

4.1. Numerical Results from BEMT and CFD

Figures 7 and 8 compare the power coefficients and thrust coefficients at different scales of HATT. All the CFD simulations were conducted using a virtual fluid corresponding to the Reynolds number appropriate for the size of each turbine. The results across various scales show that the overall trends are consistent. However, there are slight differences in the values of the power coefficient and thrust coefficient. Similarly, BEMT was performed under the same conditions as those used in the CFD simulation. For the BEMT simulations, the lift and drag coefficients were calculated using Xfoil at the Reynolds numbers corresponding to each turbine diameter. The BEMT analysis was subsequently conducted using these scale-appropriate coefficients. The results from BEMT also showed slight discrepancies between the 4 m and 20 m turbine sizes, with the BEMT results being similar to those obtained from the CFD simulation. Moreover, the scale effects between different turbine sizes are more pronounced at a low TSRs such as 1 and 2. They are also significant at high TSRs from 6 to 9. In contrast, the effects are less noticeable at TSRs near the optimal TSR range of 3 to 5. This can be attributed to the fact that at low TSRs, the blade operates at a high angle of attack, where flow separation and viscous effects are more sensitive to Reynolds number variations. Similarly, at high TSRs, the increased relative velocity amplifies the influence of the Reynolds number. These trends of scale effects can be found in the results from both CFD and BEMT.

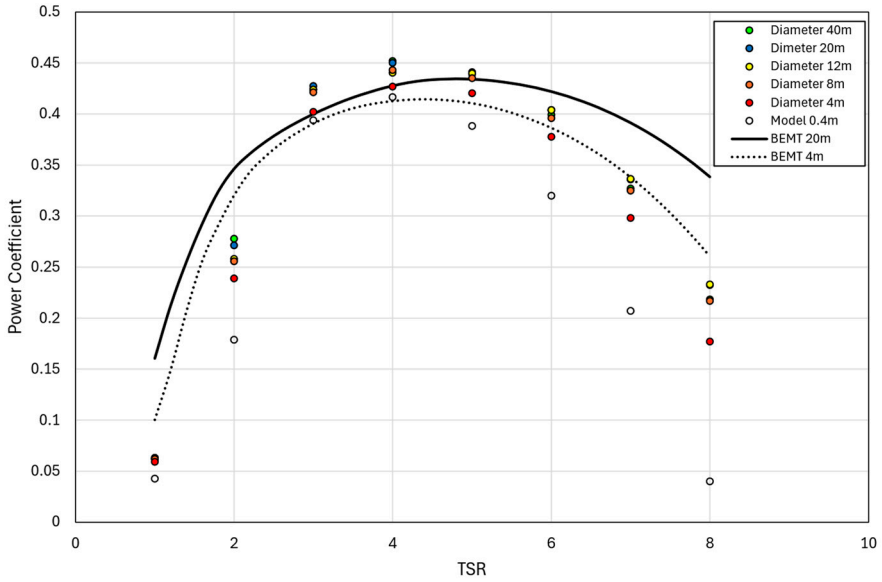

Figure 7. Comparison of power coefficients across various scales using BEMT and CFD.

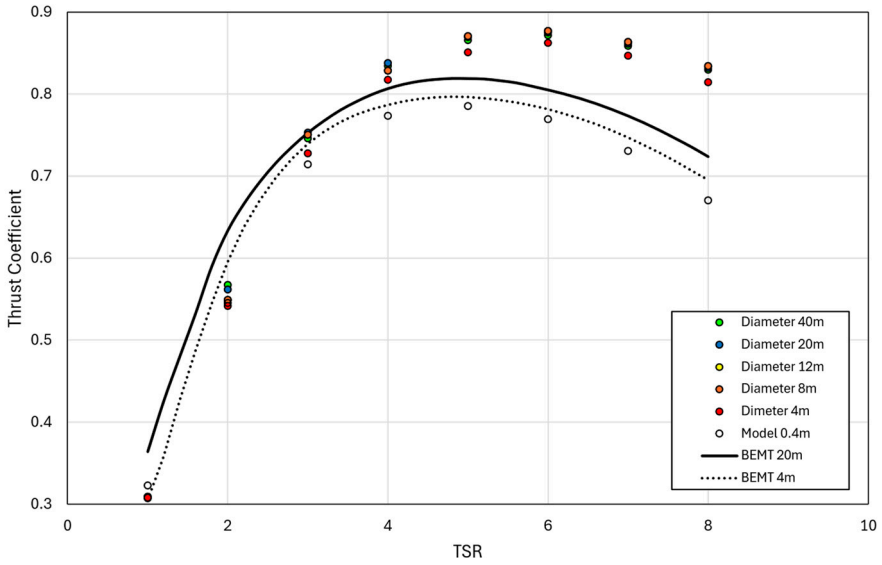

Figure 8. Comparison of thrust coefficients across various scales using BEMT and CFD.

It is important to note that the results regarding performance coefficients at the TSR range of 3 to 5 closely match between CFD and BEMT. However, the differences between CFD and BEMT are more evident at the other TSRs. In addition, the differences become larger when TSR decreases at low TSRs or increases at high TSRs. To quantify this, discrepancies between CFD and BEMT at the 20 m turbine were analysed. Near the optimal TSR, the difference ranged from 1.6% to 6.8%. In contrast, it ranged from 14% to 61% at other TSRs.

Although the same blade is used, the results differ based on the size of the turbines. This discrepancy leads to a gap between the performance predictions obtained from model and the actual power output of the full-scale turbine. The differences between different size turbines can be explained by the effects of the Reynolds number. Therefore, the numerical quantification of these distinctions and their causes will be addressed in the following sections (Sections 4.2 and 4.3).

4.2. Difference in Results with Varying Reynolds Number

Figure 9 shows the power coefficients for different turbine diameters at a TSR of 4. As turbine size increases, the power coefficient also increases. However, the differences in power coefficients between the turbines tend to decrease. In this context, Figure 10 illustrates the numerical quantification of the differences in power coefficients when the turbine size is expressed in terms of Reynolds number, compared to the largest turbine. The discrepancies between each turbine and the largest turbine range from 0.312% to 7.32%. It is noteworthy that for Reynolds numbers above 1.0×10^7, the deviation from the largest turbine is less than 1%, showing a tendency to gradually converge. The same type of results for the full range of TSRs from 1 to 8 can be found in Appendices A.1 and A.2. A similar tendency is observed across all TSRs, with only minor discrepancies at points where the power coefficient remains constant.

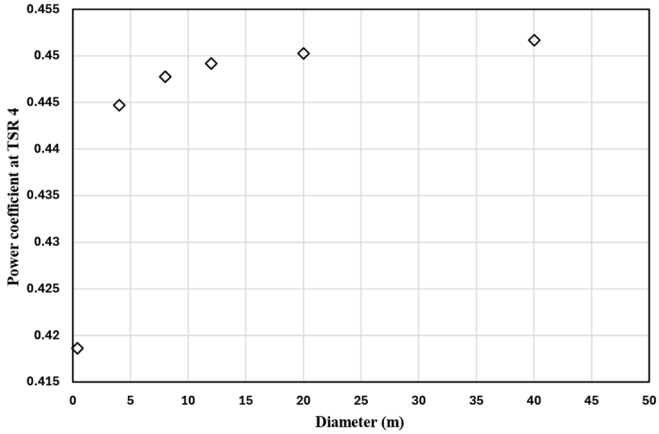

Figure 9. Comparison of C_P values at various turbines scales at TSR 4.

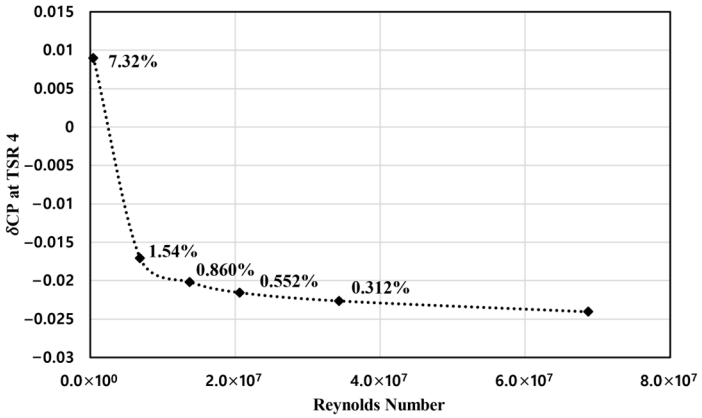

Figure 10. Numerical quantification of the differences in C_P according to Reynolds number at TSR 4.

The results for thrust coefficients which are another important assessment factor of tidal turbines show the same tendency to those of power coefficients. Figures 11 and 12 depict the result for thrust coefficients, presenting the same insights as Figures 9 and 10. As the turbine diameter increases, thrust coefficients tend to increase. This result is consistent with the result for the power coefficient. Moreover, the differences between each turbine and the largest turbine vary between 7.83% and 0.328%. The results for overall TSRs related to Figures 11 and 12 can be found in Appendices A.3 and A.4. The thrust coefficient results for the full range of TSRs showing the same tendency to converge as the Reynolds number increases can be found in Appendices A.3 and A.4. As seen from the results of the power

coefficient and thrust coefficient, the difference in performance coefficients converges to within approximately 1% for Reynolds numbers above 1.0×10^7 at the same TSR.

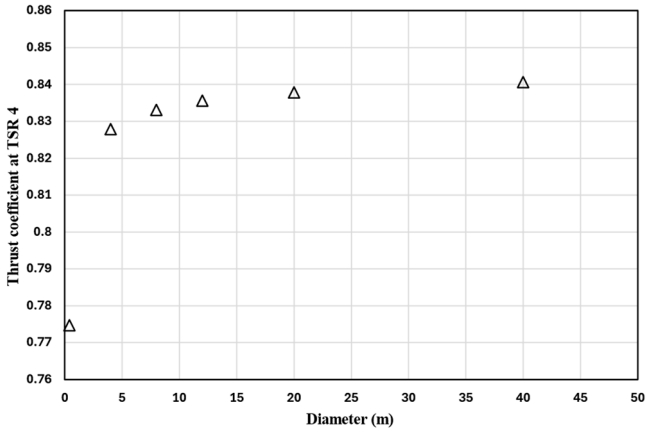

Figure 11. Comparison of C_T values at various turbine scale at TSR 4.

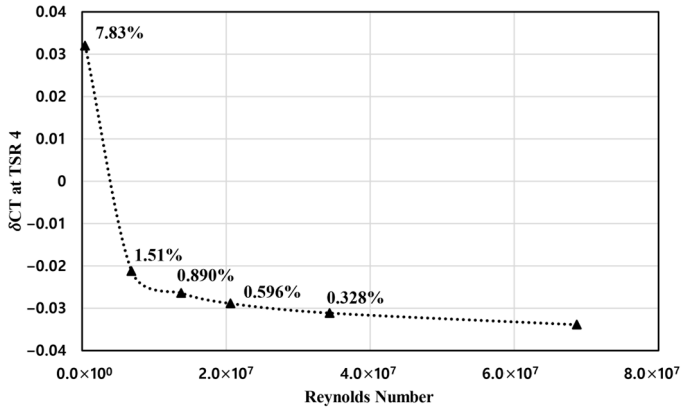

Figure 12. Numerical quantification of the differences in C_T according to Reynolds number at TSR 4.

These outcomes prove that the tidal turbine performances are affected by the Reynolds number based on the size of the turbine. However, the differences in turbine effectiveness tend to remain consistent with only minor variations when the Reynolds number exceeds 1.0×10^7. This trend is observed across all TSRs, not just specific ones.

4.3. Influence of Shear and Pressure Torque Components on Tidal Turbine Performance

The scale effects due to Reynolds number on tidal performance are observed in Section 4.2. However, scale effects differently affect various TSRs. In Figures 7 and 8, discrepancies in performance for turbines of various scales differ near the optimal TSR and at high TSRs. At high TSRs, scale effects caused by the Reynolds number are greater than at other TSRs. This can be explained by the contributions of shear and pressure torque components to tidal performance at different TSRs. Figure 13 indicates the effect of the torque components on tidal turbines, specifically for the largest and smallest turbines. The contribution of shear and pressure torque components to turbine performance is expressed through the normalised torque, which is calculated as the torque divided by $1/2\rho SV^2R$. The turbines exhibit apparently different shear and pressure moment coefficients at high TSRs. When the turbine operates at high TSRs, the smaller turbine experiences a larger moment due to shear stress than the larger turbine. As a result, the torque due to shear stress influences the decrease in turbine performance. This leads to a reduction in the total torque of the turbine.

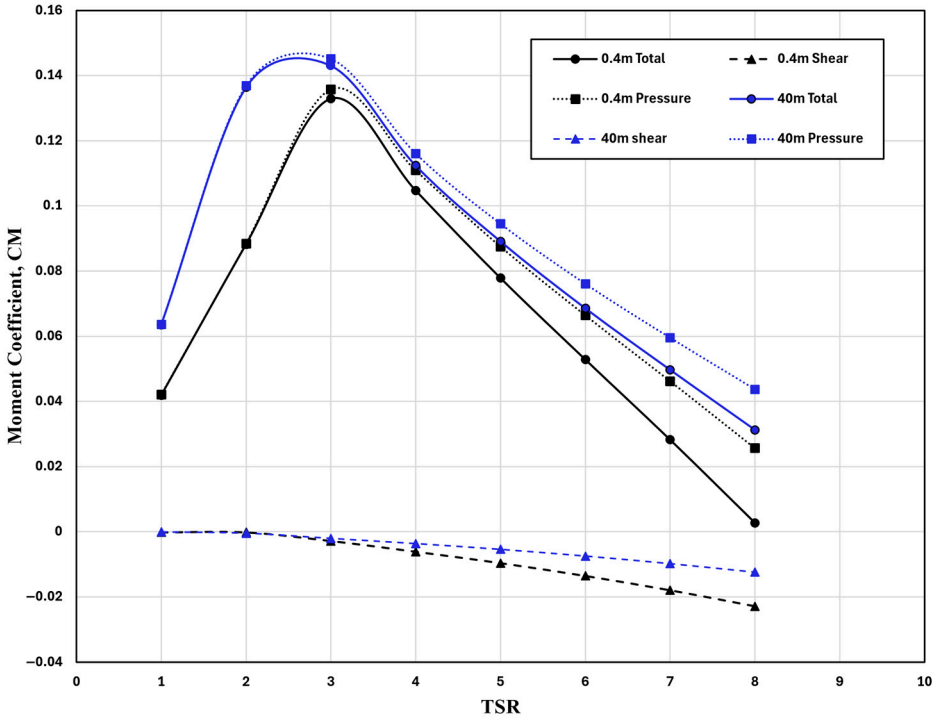

Figure 13. Torque components on different sized turbines.

Additionally, another torque factor on the turbine surface is the torque due to surface pressure. This torque decreases at high TSRs. However, the rate of reduction differs across various scales of turbines. As shown in Figure 13, the rate of decrease for the smaller turbine is greater than that for the larger turbine. This difference in surface pressure also leads to variations in turbine performance. When these results are reconsidered in relation to the Reynolds number, a turbine with a lower Reynolds number exhibits a larger shear stress torque at the turbine surfaces at high TSRs. Moreover, the rate of decrease in pressure torque is greater for the smaller turbine than for the larger turbine. As a result, this can lead to a reduction in turbine performance. In this regard, it is noted that the shear torque acts as a resistive component that opposes turbine rotation, thereby reducing overall performance, whereas the pressure torque means that a smaller turbine with a lower Reynolds number suffers from greater performance degradation due to the combined effect of higher resistive shear torque and a more rapid decrease in driving pressure torque, particularly at high TSRs. Furthermore, the values of shear and pressure torque components for different turbine sizes were quantified and summarised in Table 4.

Table 4. Moment coefficient on different sized turbines.

	Total (0.4 m)	Pressure (0.4 m)	Shear (0.4 m)	Total (40 m)	Pressure (40 m)	Shear (40 m)
TSR 1	0.0418	0.0420	−0.000209	0.0635	0.0636	−0.00009
TSR 2	0.0882	0.0884	−0.000217	0.1363	0.1368	−0.00047
TSR 3	0.1329	0.1357	−0.002859	0.1431	0.1451	−0.00207
TSR 4	0.1047	0.1108	−0.006160	0.1124	0.1161	−0.00367
TSR 5	0.0778	0.0875	−0.009659	0.0891	0.0945	−0.00545
TSR 6	0.0528	0.0664	−0.013596	0.0686	0.0761	−0.00750
TSR 7	0.0282	0.0462	−0.018003	0.0497	0.0595	−0.00984
TSR 8	0.0027	0.0256	−0.002291	0.0312	0.0437	−0.01245

4.4. Wall Shear Stress

Figure 14 shows the influence of shear stress on turbine surfaces for turbines of different sizes. The shear stress acting on the turbine surface is normalised by dividing the wall shear stress by the dynamic pressure, $1/2\rho V_{in}^2$. As shown in Figure 14, turbines of different sizes exhibit significant differences in shear stress at the same TSR. Specifically, the turbine with the smaller Reynolds number experiences higher shear stress compared to the turbine with the larger Reynolds number. At the same TSR of 4, the turbine having a smaller Reynolds number undergoes nearly twice the shear stress compared to the turbine having a larger Reynolds number. This results in a decrease in performance efficiency. Additionally, this effect of Reynolds number is consistent with the results shown in Figure 13, where the torque components were compared for turbines of different sizes.

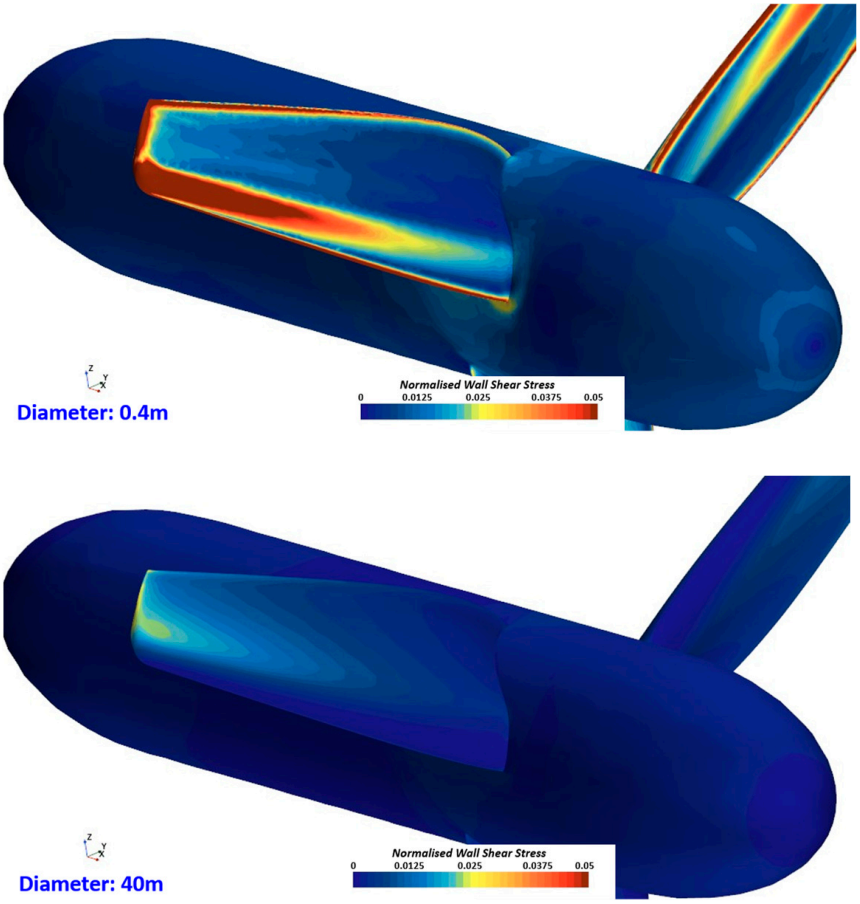

Figure 14. Shear stress distribution on turbines of different sizes at TSR 4.

4.5. Surface Pressure

Figures 15 and 16 illustrate the comparison between turbines of different scales. The surface pressure on the turbine is divided into the face-side and the backside. The face-side refers to the pressure side of the blade, where higher pressure is generated, while the backside corresponds to the suction side, where lower pressure is observed. The pressure difference between two sides generated lift, which ultimately contributes to turbine rotation and power generation. The magnitude of the surface pressure is normalised by dividing the pressure by dynamic pressure, $1/2\rho V_{in}^2$. The surface pressure on the turbine that has a large Reynolds number is smaller than on the turbine that has small Reynolds number at same TSR of 4. However, the surface pressure acting on the turbine with a large Reynolds number is larger than on the turbine with a small Reynolds number. This can be attributed to the fact that at higher Reynolds numbers, viscous effects become relatively smaller, leading to

a more favourable pressure distribution across the blade surfaces. This observation is in good agreement with the result that a larger turbine has a better efficiency at the same TSR, as shown in Figure 13.

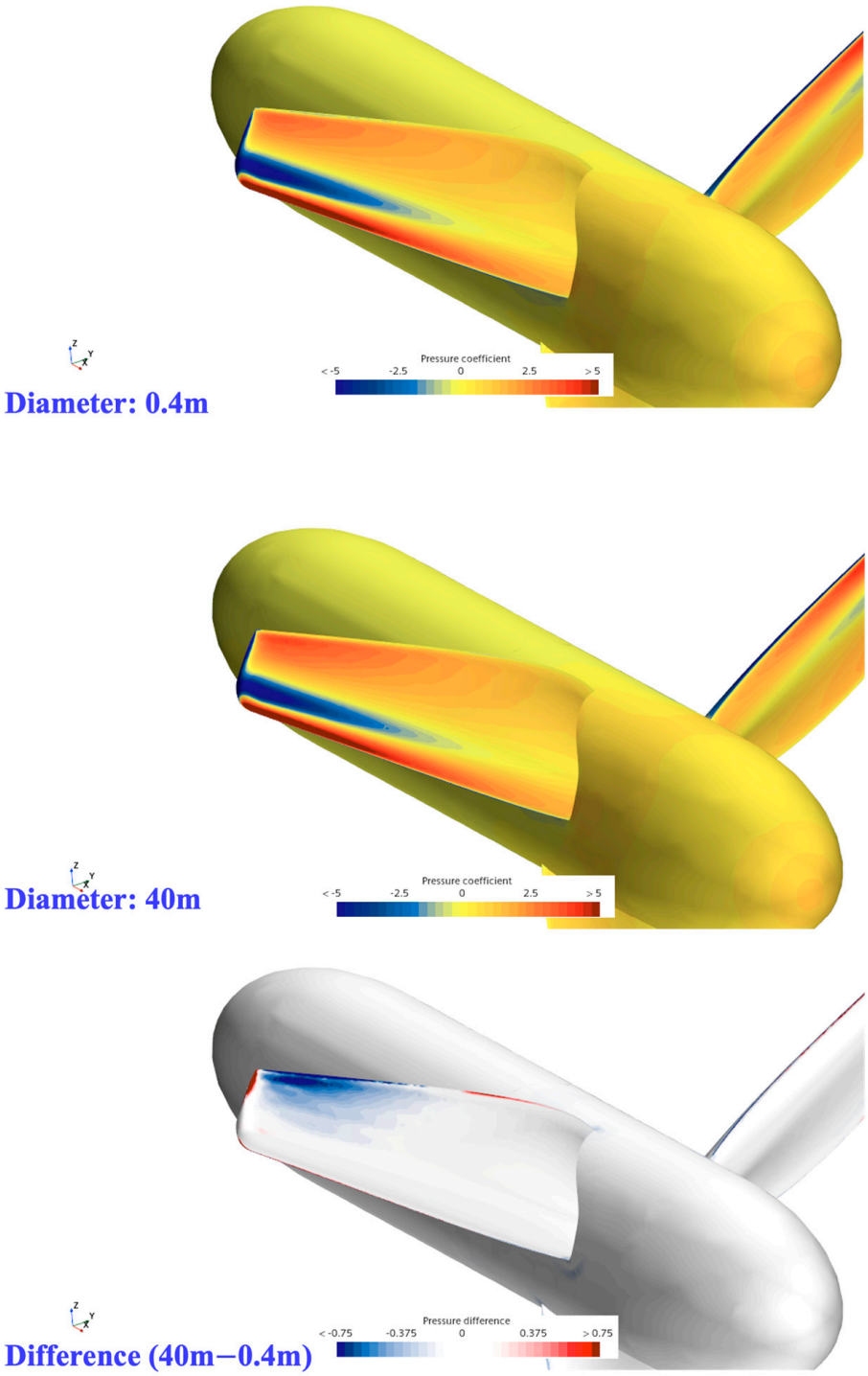

Figure 15. Pressure distribution on turbines of different sizes at TSR 4 (Face-side).

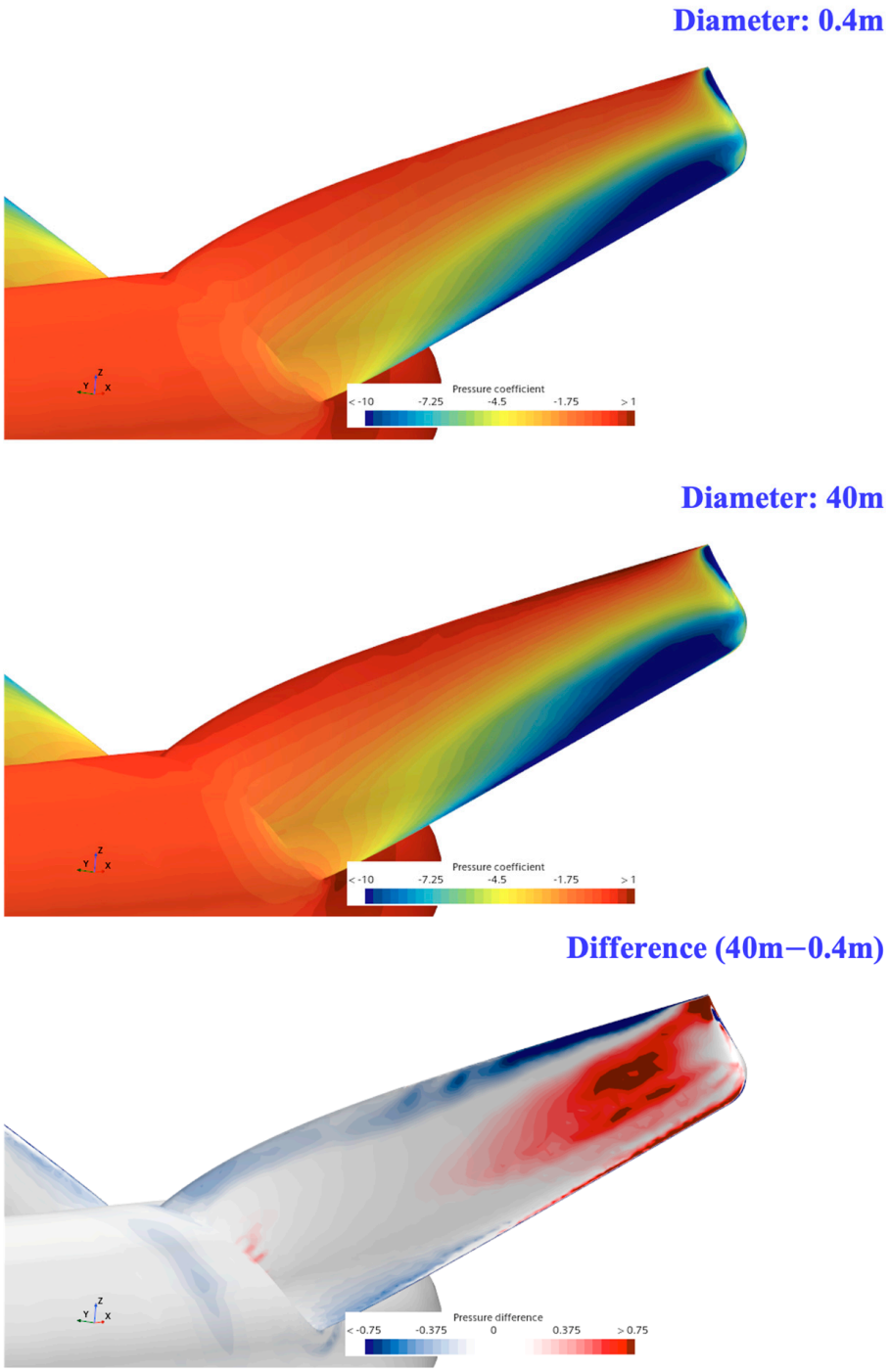

Figure 16. Pressure distribution on turbines of different sizes at TSR 4 (backside).

5. Concluding Remarks

The Reynolds number effects on tidal turbine performance were investigated using a RANS-based CFD model. The simulation results were compared with the experimental results from a previous study [25]. Satisfactory agreement was observed between the CFD predictions and experimental measurements. Moreover, a verification study was conducted to estimate the numerical uncertainties of the simulations. The numerical uncertainties in the CFD model are 0.37% for C_p and 0.27% for C_T. These results can ensure the reliability of the numerical model outcomes.

To assess the effects of the Reynolds number, the performance of tidal turbines at different scales was estimated using CFD simulations with the virtual fluid method. As a

result, the performance of the turbines varies according to Reynolds number. A turbine with a small Reynolds number has lower power efficiency than a turbine with a large Reynolds number at the same TSR. Additionally, as the Reynolds number increases, a tendency was observed where the difference between turbines with different Reynolds number decreases. This tendency is shown across all TSRs.

In this paper, discrepancies caused by the effects of the Reynolds number are quantitatively evaluated. They are calculated to range from 0.312% to 7.32% according to the Reynolds number at the same TSR. The quantified results across all TSRs are shown in Appendices A.2 and A.4. Interestingly, above a Reynolds number of 1.0×10^7, the performance coefficients show only minor discrepancies with differences of around 1%. This convergence can be attributed to the lift and drag coefficients of the airfoil becoming less sensitive to further increase in the Reynolds number, leading to stabilisation of turbine performance.

Furthermore, the underlying causes of Reynolds number effects on tidal turbine performance were identified through detailed analysis of torque components acting on the turbine blade surfaces. In a comparison between turbines with different Reynolds numbers, the turbine with a small Reynolds number has a higher magnitude of shear stress on its surfaces than the turbine with a larger Reynolds number. Moreover, the surface pressure is lower on the turbine with a small Reynolds number than on the turbine with a large Reynolds number.

The reason for increasing power loss due to the effects of the Reynolds number at higher TSRs is also explained by investigating the components of torque. The difference in shear stress between turbines with different Reynolds numbers increases as TSR increases. Furthermore, the rate of decrease in surface pressure is larger at higher TSRs. These results amplify the effects of the Reynolds number in the higher TSR regions.

In summary, the virtual fluid method was employed to systematically evaluate scale effects across a wide range of turbine size under varying Reynolds numbers. The Reynolds number-dependent performance discrepancies were quantitatively assessed, and the underlying causes were identified through decomposition of torque into shear and pressure components. The effects of the Reynolds number were estimated by changing the sizes of the turbines. Above a Reynolds number of 1.0×10^7, the performance efficiency of the turbines shows a 1% discrepancy between different sized turbine. These quantified results are expected to serve as practical design indicators that can be considered in the early stages of tidal turbine development, contributing to more accurate full-scale performance prediction. It is hoped that utilising such quantitative indicators will help accurately predict turbine performance, which varies according to Reynolds number. Lastly, to further establish the effect of the Reynolds number on various types of turbines, research is recommended on different types of turbines such as vertical type turbines, turbines with duct, and floating tidal turbines. Moreover, the present work evaluated the effect of Reynolds number on blades with a single type of airfoil. In this regard, a previous study demonstrated that blade shape significantly influences the surrounding flow characteristics [31]. Under this assumption, blades with various airfoil types may yield different numerical results, which warrants further investigation.

All simulations were performed using Intel Xeon Gold processors with a total of 52 cores.

Author Contributions: Conceptualization, S.S.; Methodology, G.M. and S.S.; Software, G.M.; Validation, G.M.; Formal analysis, G.M., H.Y. and Y.D.; Investigation, G.M., H.Y. and S.S.; Data curation, G.M. and K.K.; Writing—original draft preparation, G.M.; Writing—review and editing, W.S., D.K. and S.S.; Visualization, G.M. and S.S.; Supervision, S.S.; Project administration, D.K. and S.S.; Funding acquisition, S.S. All authors have read and agreed to the published version of the manuscript.

Funding: This research was funded by Inha University Research Grant.

Data Availability Statement: The data presented in this study are available on request from the corresponding author.

Conflicts of Interest: The authors declare no conflict of interest.

Appendix A

Appendix A.1. Comparison of C_P Values at Various Turbine Scales

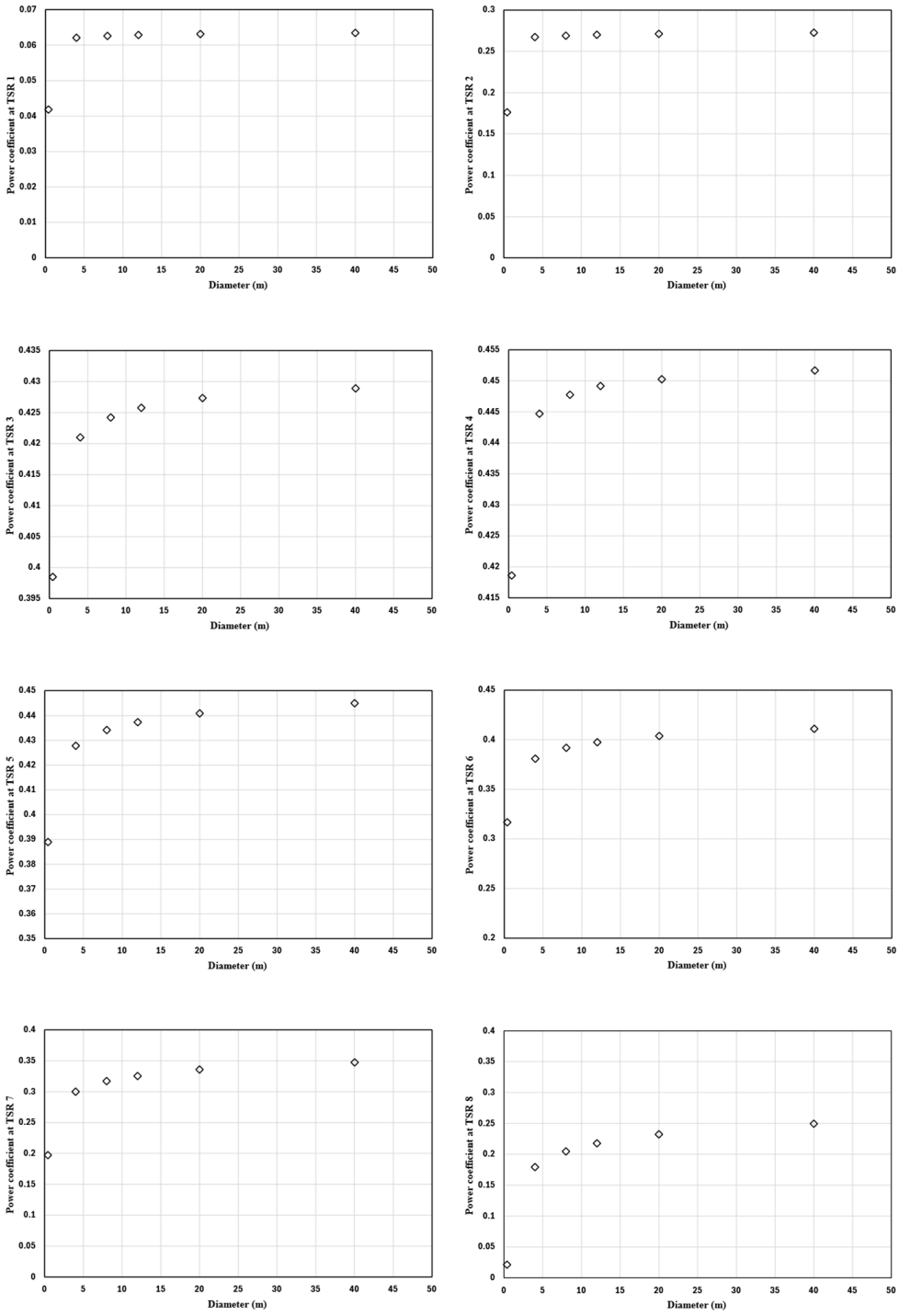

Appendix A.2. Numerical Quantification of the Differences in C_P According to Reynolds Number

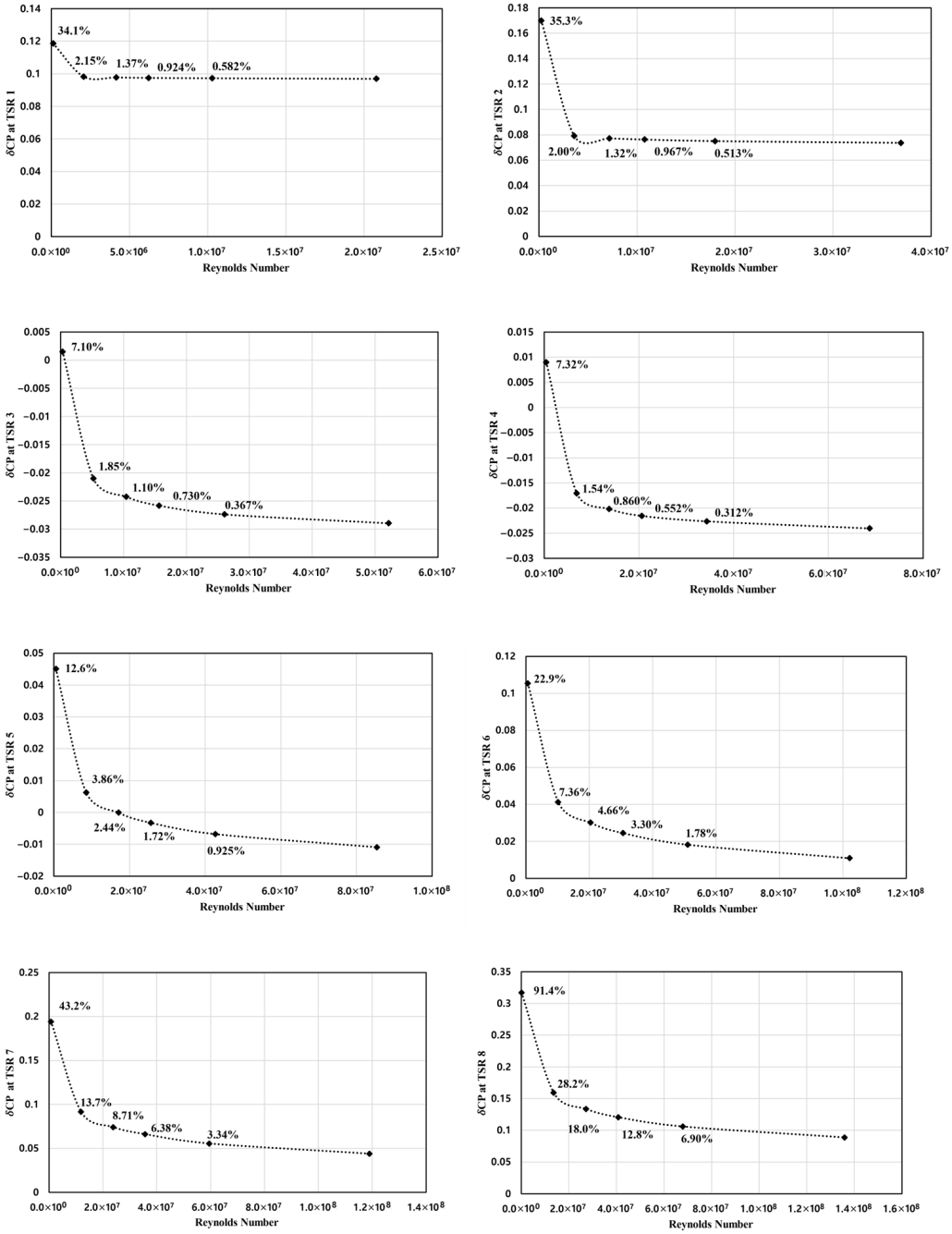

Appendix A.3. Comparison of C_T Values at Various Turbine Scales

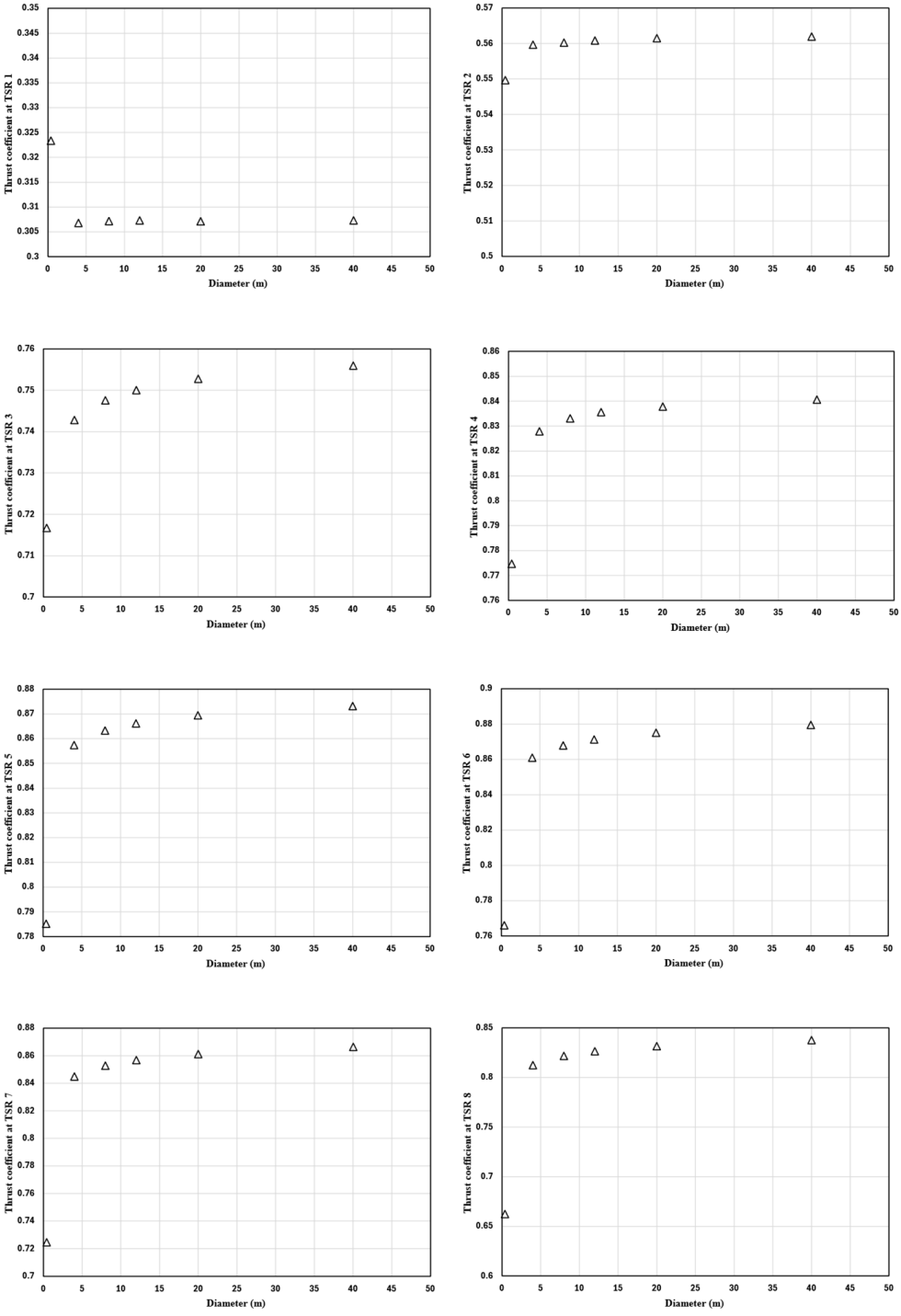

Appendix A.4. Numerical Quantification of the Differences in C_T According to Reynolds Number

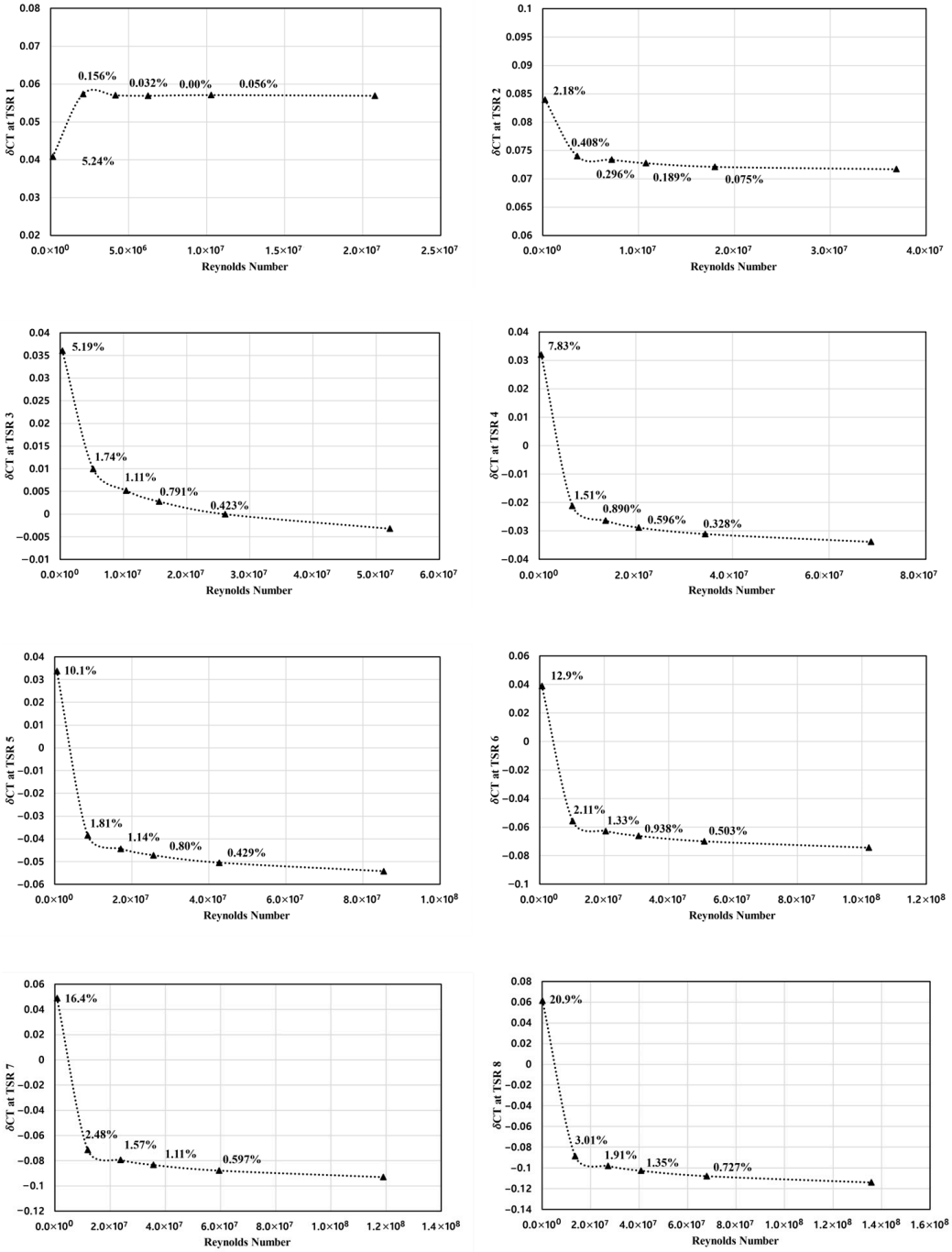

References

1. Nachtane, M.; Tarfaoui, M.; Goda, I.; Rouway, M. A review on the technologies, design considerations and numerical models of tidal current turbines. *Renew. Energy* **2020**, *157*, 1274–1288. [CrossRef]
2. Munko, M.J.; Camacho, M.A.V.; Cuthill, F.; Brádaigh, C.M.Ó.; Dubon, S.L. Efficient reconstruction of high-resolution tidal turbine blade deflection and strain maps through sensing location optimisation. *J. Mar. Sci. Eng.* **2026**, *14*, 408. [CrossRef]
3. Ye, D.; Wang, T.; Fan, Q.; Xue, T. A New Probabilistic Approach to Fault Detection for Tidal Stream Turbine Blades. *J. Mar. Sci. Eng.* **2026**, *14*, 721. [CrossRef]
4. Scandura, P.; Mauro, S.; Messina, M.; Brusca, S. Numerical Simulations and Experimental Tests for Tailored Tidal Turbine Design. *J. Mar. Sci. Eng.* **2026**, *14*, 236. [CrossRef]
5. Jung, S.; Lee, H.; Jang, I.S.; Moon, S.M.; Kim, H.; Seo, C.H.; Kim, J.; Ko, J.H. Investigation on Wake Characteristics of Two Tidal Stream Turbines in Tandem Using a Mobile Submerged PIV System. *J. Mar. Sci. Eng.* **2026**, *14*, 135. [CrossRef]
6. Qian, Y.; Zhang, Y.; Sun, Y.; Zhang, H.; Zhang, Z.; Li, C. Experimental and numerical investigations on the performance and wake characteristics of a tidal turbine under yaw. *Ocean Eng.* **2023**, *289*, 116276. [CrossRef]
7. Guo, X.; Yang, J.; Gao, Z.; Moan, T.; Lu, H. The surface wave effects on the performance and the loading of a tidal turbine. *Ocean Eng.* **2018**, *156*, 120–134. [CrossRef]
8. Allsop, S.; Peyrard, C.; Thies, P.R.; Boulougouris, E.; Harrison, G.P. Hydrodynamic analysis of a ducted, open centre tidal stream turbine using blade element momentum theory. *Ocean Eng.* **2017**, *141*, 531–542. [CrossRef]
9. Ellis, R.; Allmark, M.; O'Doherty, T.; Mason-Jones, A.; Ordonez-Sanchez, S.; Johannesen, K.; Johnstone, C. Design process for a scale horizontal axis tidal turbine blade. In Proceedings of the 4th Asian Wave and Tidal Energy Conference, Taipei, Taiwan, 9–13 September 2018.
10. Masters, I.; Chapman, J.C.; Willis, M.R.; Orme, J.A.C. A robust blade element momentum theory model for tidal stream turbines including tip and hub loss corrections. *J. Mar. Eng. Technol.* **2014**, *10*, 25–35. [CrossRef]
11. Snel, H.; Houwink, R.; Piers, W. *Sectional Prediction of 3D Effects for Separated Flow on Rotating Blades*; National Technical Reports Library: Alexandria, VA, USA, 1992.
12. Mannion, B.; Leen, S.B.; Nash, S. Development and assessment of a blade element momentum theory model for high solidity vertical axis tidal turbines. *Ocean Eng.* **2020**, *197*, 106918. [CrossRef]
13. Song, S.; Demirel, Y.K.; Atlar, M.; Shi, W. Prediction of the fouling penalty on the tidal turbine performance and development of its mitigation measures. *Appl. Energy* **2020**, *276*, 115498. [CrossRef]
14. Yan, J.; Deng, X.; Korobenko, A.; Bazilevs, Y. Free-surface flow modeling and simulation of horizontal-axis tidal-stream turbines. *Comput. Fluids* **2017**, *158*, 157–166. [CrossRef]
15. Khalid, A.; Khaled, F.; Guillou, S.S. Study of the Effects of Waves on the Evolution of Scour Under a Tidal Turbine by Two-Phase Numerical Modeling. *J. Mar. Sci. Eng.* **2026**, *14*, 308. [CrossRef]
16. Min, G.; Choi, W.; Yun, H.; Do, Y.; Kim, K.; Shi, W.; Dai, S.; Kim, D.; Song, S. Evaluation of Free-Surface Exposure Effects on Tidal Turbine Performance Using CFD. *J. Mar. Sci. Eng.* **2025**, *13*, 1589. [CrossRef]
17. Koh, W.; Ng, E. Effects of Reynolds number and different tip loss models on the accuracy of BEM applied to tidal turbines as compared to experiments. *Ocean Eng.* **2016**, *111*, 104–115. [CrossRef]
18. El-Shahat, S.A.; Li, G.; Lai, F.; Fu, L. Investigation of parameters affecting horizontal axis tidal current turbines modeling by blade element momentum theory. *Ocean Eng.* **2020**, *202*, 107176. [CrossRef]
19. Stringer, R.M.; Hillis, A.J.; Zang, J. Numerical investigation of laboratory tested cross-flow tidal turbines and Reynolds number scaling. *Renew. Energy* **2016**, *85*, 1316–1327. [CrossRef]
20. Mason-Jones, A.; O'Doherty, D.M.; Morris, C.E.; O'Doherty, T.; Byrne, C.B.; Prickett, P.W.; Grosvenor, R.I.; Owen, I.; Tedds, S.; Poole, R.J. Non-dimensional scaling of tidal stream turbines. *Energy* **2012**, *44*, 820–829. [CrossRef]
21. Makhali, O.Z.; Nugroho, P.N.A.; Tiyasmihadi, T. Design of Floating Tidal Energy. In *Smart Innovation in Green and Sustainable Energy: Select Proceedings of ICOME 2023, 30–31 August, Bali, Indonesia*; Springer: Berlin/Heidelberg, Germany, 2025; Volume 1279, p. 285.
22. Ferziger, J.H.; Perić, M.; Street, R.L. *Computational Methods for Fluid Dynamics*; Springer: Berlin/Heidelberg, Germany, 2019.
23. Menter, F.R. Two-equation eddy-viscosity turbulence models for engineering applications. *AIAA J.* **1994**, *32*, 1598–1605. [CrossRef]
24. Wang, D.; Atlar, M.; Sampson, R. An experimental investigation on cavitation, noise, and slipstream characteristics of ocean stream turbines. *Proc. Inst. Mech. Eng. Part A J. Power Energy* **2007**, *221*, 219–231. [CrossRef]
25. Shi, W.; Rosli, R.; Atlar, M.; Norman, R.; Wang, D.; Yang, W. Hydrodynamic performance evaluation of a tidal turbine with leading-edge tubercles. *Ocean Eng.* **2016**, *117*, 246–253. [CrossRef]
26. Kim, K.-W.; Paik, K.-J.; Lee, J.-H.; Song, S.-S.; Atlar, M.; Demirel, Y.K. A study on the efficient numerical analysis for the prediction of full-scale propeller performance using CFD. *Ocean Eng.* **2021**, *240*, 109931. [CrossRef]
27. Machado, L.d.V.; Fernandes, A.C. Proposals to Improve Load and Cavitation Computational Fluid Dynamics Analysis With Moving Reference Frame of a Conventional Propeller. *J. Offshore Mech. Arct. Eng.* **2021**, *143*, 021901. [CrossRef]

28. Song, S.; Demirel, Y.K.; Atlar, M. An Investigation Into the Effect of Biofouling on Full-Scale Propeller Performance Using CFD. In Proceedings of the OMAE2019, 38th International Conference on Ocean, Offshore & Arctic Engineering, Glasgow, UK, 9–14 June 2019.
29. Richardson, L.F., IX. The approximate arithmetical solution by finite differences of physical problems involving differential equations, with an application to the stresses in a masonry dam. *Philos. Trans. R. Soc. Lond. Ser. A Contain. Pap. A Math. Or Phys. Character* **1911**, *210*, 307–357. [CrossRef]
30. Celik, I.B.; Ghia, U.; Roache, P.J.; Freitas, C.J.; Coleman, H.; Raad, P.E. Procedure for Estimation and Reporting of Uncertainty Due to Discretization in CFD Applications. *J. Fluids Eng.* **2008**, *130*, 078001. [CrossRef]
31. Turkyilmazoglu, M.; Alotaibi, A. Coating with Newtonian fluid by a two-parameter blade family leading to exact dynamic and thermal solutions. *Chin. J. Phys.* **2025**, *96*, 1191–1202. [CrossRef]